Structure
Article

Cell
PRESS

The Complete VS Ribozyme in Solution Studied by Small-Angle X-Ray Scattering

Jan Lipfert,[1,5] Jonathan Ouellet,[2,5] David G. Norman,[2] Sebastian Doniach,[1,3,4] and David M.J. Lilley[2,*]
[1]Department of Physics, Geballe Laboratory of Advanced Materials, Stanford University, Stanford, CA 94305, USA
[2]Nucleic Acid Structure Research Group, Cancer Research UK, MSI/WTB Complex, The University of Dundee, Dundee DD1 5EH, UK
[3]Departments of Applied Physics and Physics
[4]Biophysics Program
Stanford University, Stanford, CA 94305, USA
[5]These authors contributed equally to this work
*Correspondence: d.m.j.lilley@dundee.ac.uk
DOI 10.1016/j.str.2008.07.007

SUMMARY

We have used small-angle X-ray solution scattering to obtain ab initio shape reconstructions of the complete VS ribozyme. The ribozyme occupies an electron density envelope with an irregular shape, into which helical sections have been fitted. The ribozyme is built around a core comprising a near-coaxial stack of three helices, organized by two three-way helical junctions. An additional three-way junction formed by an auxiliary helix directs the substrate stem-loop, juxtaposing the cleavage site with an internal loop to create the active complex. This is consistent with the current view of the probable mechanism of *trans*-esterification in which adenine and guanine nucleobases contributed by the interacting loops combine in general acid-base catalysis.

INTRODUCTION

RNA catalysis is exploited in various cell types for the splicing of mRNA and rRNA and the maturation of tRNA, the control of gene expression, and the synthesis of proteins (Lilley and Eckstein, 2008). The nucleolytic ribozymes bring about site-specific cleavage of the phosphodiester backbone by nucleophilic attack of the 2′ hydroxyl on the adjacent 3′ phosphorus to create a 2′,3′ cyclic phosphate and the reverse ligation reaction. The members of this class adopt markedly different folds, although all are based either on helical junctions or complex pseudoknots.

The Varkud satellite (VS) ribozyme (Saville and Collins, 1990) is the largest of the known nucleolytic ribozymes, and the only one for which there is no crystal structure. Analysis of the secondary structure showed that it comprises six helical sections (Beattie et al., 1995) (Figure 1; helices I–VI). The 5′ stem-loop contains the cleavage site and can be considered the substrate. This can be physically disconnected from the remaining section, which then behaves as a *trans*-acting ribozyme (Guo and Collins, 1995; McLeod and Lilley, 2004). The five helices of the *trans* ribozyme are connected by two three-way junctions, the lower junction comprising helices II-III-VI and the upper junction of helices

III-IV-V. Jones et al. (2001) pointed out that the natural ribozyme is also likely to have an additional helix (VII) that forms a three-way junction with helices I and II. The secondary structure of the junction has not been determined, but it was shown that this form of the ribozyme was an efficient ligase, suggesting that the inclusion of helix VII stabilizes the active fold of the ribozyme.

In previous work, we have analyzed the structure of the five-helix *trans*-acting ribozyme via independent analysis of its component junctions using electrophoresis and fluorescence resonance energy transfer (FRET). We found that both isolated junctions undergo two-state folding transitions induced by the addition of divalent metal ions, and we were able to propose global structures for the folded form of each (Lafontaine et al., 2001a, 2002). Such junctions commonly fold by the coaxial association of two helices (Lescoute and Westhof, 2006), and we proposed that helices III and VI, and helices III and IV, are coaxial in the lower and upper junctions, respectively, with acute angles subtended between helices II and VI and between helices V and III. In the intact ribozyme the two junctions associate through the common helix III, leading to a coaxial alignment of helices IV through III to VI, from which helices II and V radiate laterally. We determined the dihedral angle between helices II and V to be approximately 80° using an electrophoretic analysis in which the length of helix III was systematically varied (Lafontaine et al., 2002).

In the natural form of the ribozyme the substrate and helix II are connected by three nucleotides, and Collins and coworkers (Rastogi et al., 1996) have shown that terminal loops of the substrate and helix V are base paired together. This localizes the substrate to the cleft formed between helices II and VI (Lafontaine et al., 2002).

Current evidence suggests that the catalytically active geometry is generated by an intimate association of the substrate internal loop with the internal loop of helix VI that contains A730. Within these two loops, two key nucleobases are strong candidates for a catalytic role: A756 in the A730 loop (Lafontaine et al., 2001b, 2002; Sood and Collins, 2002; Jones and Strobel, 2003; Hiley et al., 2002; Zhao et al., 2005), and G638 in the substrate loop (Wilson et al., 2007).

Significant efforts to crystallize the VS ribozyme in a number of laboratories have been unsuccessful to date, and thus all our
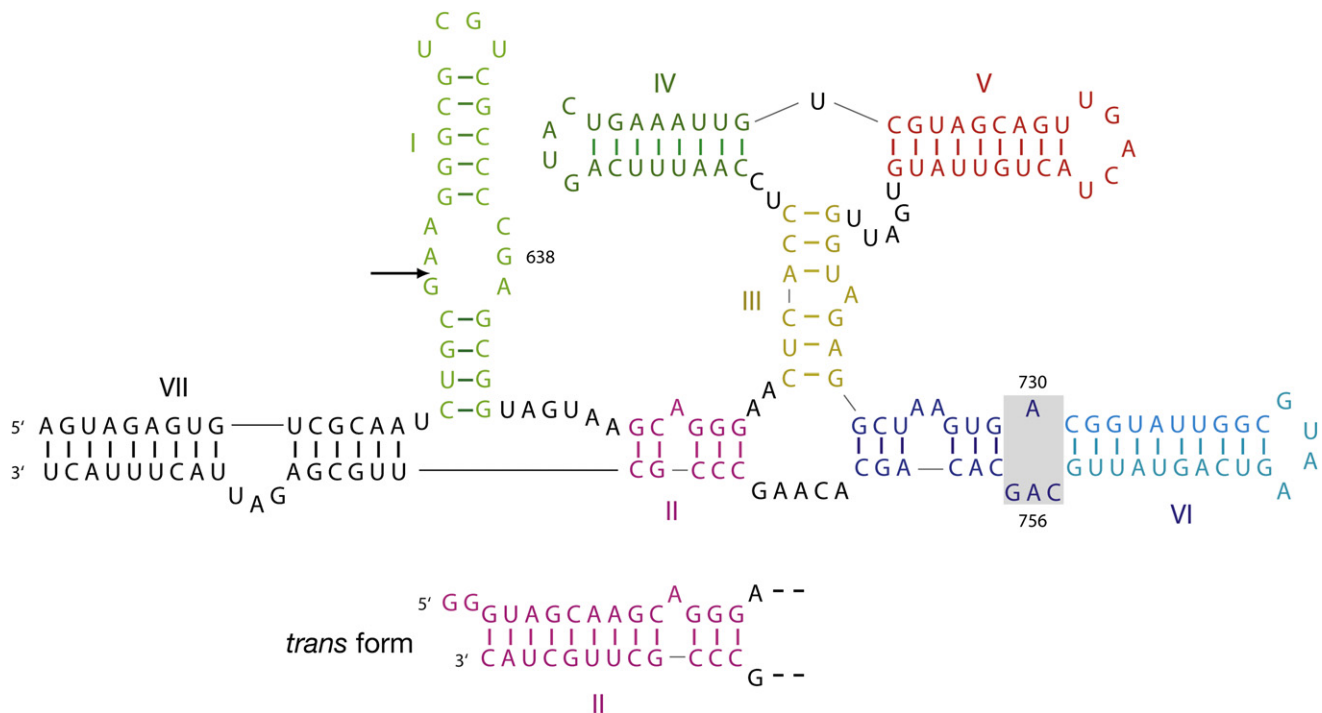
Figure 1. The Sequence and Secondary Structure of the VS Ribozyme

The full sequence shown is that of the *cis*-acting ribozyme, with helix VII that forms a third three-way junction. Helix VII was absent from the majority of *cis* forms of the ribozyme previously studied, for which the 5′ terminus would be located in helix I. The secondary structure of the I-II-VII junction is not well defined, because in principle it can branch migrate over four steps, potentially transferring up to four base pairs from the end of helix II to the end of helix VII. The helices are differentiated by color; this scheme is used throughout the paper. The arrow shows the position of ribozyme cleavage in the internal loop of helix I, and the A730 loop is shaded. Helix III is shown in its natural form with a bulged adenine; in the SAXS experiments, this helix has been replaced with a fully paired 7 bp helix. The *trans* form of the ribozyme lacks helices I and VII, and has the lengthened helix II shown; only helix II is shown, because the rest of the ribozyme is identical. Full sequences for all the constructs analyzed in these studies are presented in Supplemental Data.

current models of the ribozyme are based on the "divide and conquer" approach, where the structure is deduced as the sum of its parts. Here we present small-angle X-ray scattering (SAXS) data on the complete VS ribozyme in solution and of several modified constructs. SAXS provides structural information on biological macromolecules in solution (Svergun and Koch, 2003; Lipfert and Doniach, 2007). The scattering data indicate that the ribozyme folds in the presence of divalent metal ions into an elongated structure that is consistent with the coaxial alignment of helices IV-III-VI. Using ab initio shape reconstruction algorithms (Svergun, 1999), low-resolution electron density maps of the folded ribozyme constructs were obtained. We present a consistent model for the complete VS ribozyme including helix VII and the docked substrate helix I. Our model places the substrate and A730 loops in close proximity, consistent with the proposed mechanism of catalysis (Wilson et al., 2007).

RESULTS AND DISCUSSION

RNA Constructs Analyzed by X-Ray Scattering in Solution

The sequence and secondary structure of the complete VS ribozyme are shown in Figure 1. We have analyzed the solution shape of the ribozyme in this form, and of subcomponents of the structure; full sequences of all constructs used are shown

in Figure S1 available online. These include the simple *trans*-acting form comprising helices II–VI, including variants in which helices IV or VI were lengthened, and the isolated junctions II-III-VI and III-IV-V with helices of 8, 5, and 13 bp and 10, 5, and 8 bp, respectively. We also studied the *cis*-acting form of the ribozyme lacking helix VII and thus the additional three-way junction. However, inclusion of helix VII provided data that could be analyzed with greater confidence and we therefore did not pursue the simpler *cis*-acting form further.

SAXS profiles were obtained as described in Experimental Procedures. Profiles for a given construct obtained at different RNA concentrations are superimposable after rescaling by forward scattering intensity (Figure S2), indicating the absence of significant aggregation or interparticle interference effects. Furthermore, the forward scattering intensity increases linearly with increasing RNA concentration and the molecular mass determined by comparing the forward scattering intensity to a molecular mass standard was in good agreement with that calculated from the RNA sequence (see Figure S2 and Table S1), within experimental errors.

Ribozyme Folding Induced by Mg²⁺ Ions

We have recorded small-angle X-ray scattering profiles for the complete *cis*-acting ribozyme (hereafter termed the *cis* form) and the simpler *trans*-acting (*trans*) form as a function of Mg²⁺
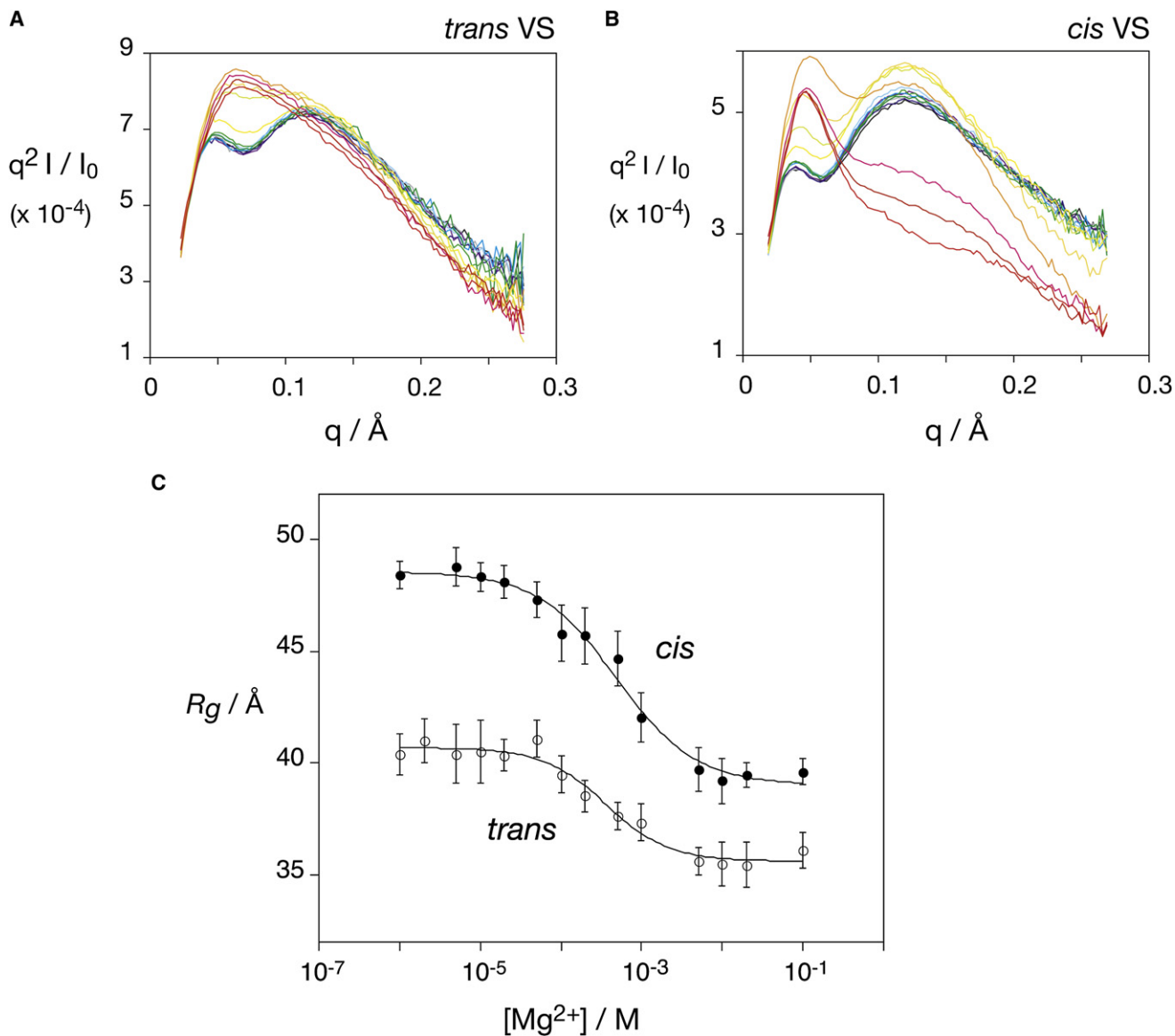
Figure 2. Folding of the _trans_ and _cis_ VS Ribozyme Constructs Monitored by SAXS

(A and B) Scattering profiles of the _trans_ VS (A) and _cis_ VS (B) ribozymes shown in Kratky representation (q^2 I as a function of q). The profiles are color coded by Mg^{2+} concentration: 0 (black), 1 (gray), 2 (purple), 5 (dark blue), 10 (light blue), 20 (cyan), and 50 (dark green) μM, 0.1 (light green), 0.2 (yellow), 0.5 (pale yellow), 1 (ochre), 5 (orange), 10 (magenta), 20 (dark red), and 100 (red) mM.

(C) Radii of gyration as a function of Mg^{2+} concentration for the _trans_ VS (open circles) and _cis_ VS ribozyme (closed circles). R_g values are obtained from the regularized transforms $P(r)$ of the scattering profiles (see Experimental Procedures). Data points and error bars at 0 and 10 mM Mg^{2+} are the mean and standard deviation of at least four independent repeats. The data points at other Mg^{2+} concentrations are from single measurements; their error bars reflect the intrinsic uncertainty of the measurement, determined from R_g fits with slightly different fitting ranges. Fits of the data to the Hill equation (Equation 1) are shown as solid lines.

concentration (see Figures 2A and 2B). The scattering profiles are presented in Kratky representation (q^2 I as a function of q; I is the intensity of scattered X-rays at a given q, q is the magnitude of the momentum transfer vector given by $4\pi \sin\theta/\lambda$ where 2θ is the scattering angle, and λ is the X-ray wavelength), which is particularly sensitive to structural transitions of biological macromolecules (Doniach, 2001). The shape of the scattering profiles for both ribozyme constructs changes significantly as a function of Mg^{2+} concentration. At low ionic concentration the profiles are bimodal, with a large peak at q ~0.12 Å^{-1}, but as the concentration increases the profiles for both the _trans_ and _cis_ ribozymes become dominated by single peaks at q = 0.068 Å^{-1} and q = 0.048 Å^{-1}, respectively.

From the scattering profiles, we have determined the radii of gyration (R_g; see Experimental Procedures) as a function of Mg^{2+} concentration. Both _cis_ and _trans_ ribozymes exhibit a systematic decrease in R_g with Mg^{2+} concentration (Figure 2C), consistent with an ion-induced folding transition into a more

Table 1. Geometrical Parameters for VS Ribozyme Constructs under Different Solution Conditions Measured by SAXS

Construct	Mg^{2+} Concentration (mM)	R_g (Å)	D_{max} (Å)
trans	0	40.5 ± 1	115 ± 5
trans	10	35.5 ± 1	110 ± 5
trans; IV + 10 bp	10	44.5 ± 1	140 ± 5
trans; VI + 11 bp	10	46.0 ± 2	150 ± 5
cis	0	49.0 ± 2	150 ± 5
cis	10	39.0 ± 1	120 ± 5
III-IV-V junction	10	28.0 ± 1	70 ± 5
II-III-VI junction	10	25.0 ± 1	85 ± 5

The radii of gyration (R_g) and the maximum intramolecular distances (D_{max}) were obtained from regularized transforms $P(r)$.

compact structure. The R_g values are well fitted by simple two-state Hill models (Figure 2, solid lines) given by

$$R_g^2\left([Mg^{2+}]\right) = R_{g,U}^2 + \left(R_{g,F}^2 - R_{g,U}^2\right)\frac{[Mg^{2+}]^n}{K_{mid}^n + [Mg^{2+}]^n}, \quad (1)$$

where $R_{g,U}$ and $R_{g,F}$ are the radii of gyration of the unfolded and folded conformations, respectively, n is the Hill coefficient, and K_{mid} is the Mg^{2+} midpoint. The radii of gyration for the unfolded (0 mM Mg^{2+}) and folded conformations ($\geq$10 mM Mg^{2+}) are shown in Table 1. Fits to Equation 1 give Hill coefficients of n = 1.2 ± 0.2 for the *trans* ribozyme and 1.1 ± 0.2 for the *cis* ribozyme. The midpoints of the transitions are K_{mid} = 0.32 ± 0.1 and 0.33 ± 0.2 mM Mg^{2+} for the *trans* and *cis* ribozymes, respectively. We have also measured radii of gyration for the isolated III-IV-V and II-III-VI junctions as a function of Mg^{2+} concentration, observing transition midpoints in the range 0.2–0.4 mM (data not shown).

The fitted Hill coefficients close to unity are indicative of relatively uncooperative transitions. The folding midpoints in the range of ~0.3 mM Mg^{2+} are very close to the midpoints determined for the isolated three-way junction III-IV-V using FRET and similar to the midpoints determined for the II-III-VI junction (Lafontaine et al., 2001a, 2002), suggesting that the folding behavior of the ribozyme is to some degree the sum of its junctions. However, the transitions are not strictly two state, and analysis of the full scattering profiles obtained as a function of Mg^{2+} concentration by singular value decomposition indicates that there are intermediates in the folding pathway. These might reflect the folding of the two junctions at slightly different Mg^{2+} concentrations, and folding and substrate docking in the *cis* ribozyme might occur with different midpoints.

We shall discuss the ion-dependent folding of the VS ribozyme in greater depth in a future publication. In what follows, we will restrict ourselves primarily to the analysis of the structure of the ribozyme and its components folded in the presence of Mg^{2+} ions. Because the scattering profiles do not change significantly at Mg^{2+} concentrations in excess of 10 mM, the data collected in the presence of 10 mM Mg^{2+} are analyzed in the following sections.

Solution Structure Determined by Ab Initio Shape Reconstructions

To determine the shape of the full ribozyme and its isolated subcomponents in solution, we employed the 3D structure re-

construction program DAMMIN (Svergun, 1999). DAMMIN reconstructs low-resolution electron density maps assembled from dummy atoms by refinement against SAXS data using a simulated annealing procedure. We have recently demonstrated the applicability of DAMMIN to low-resolution RNA structure determination for several test cases of known structure (Lipfert et al., 2007a). Details of the procedure are described in Experimental Procedures. In brief, for each RNA construct, we generated ten independent DAMMIN reconstructions each for at least three different experimental scattering profiles. The ten independent models were compared using the software DAMAVER (Volkov and Svergun, 2003), giving reproducible results in all cases as judged by the normalized spatial discrepancy criterion (see Experimental Procedures; a superposition of individual models is shown in Figure S3). The ten independent models were superimposed and a filtered consensus model was generated. Consensus models generated from repeat experimental scattering profiles for the same construct gave similar results. All the reconstructions, maps, and models derived here are presented at http://www.dundee.ac.uk/biocentre/nasg/vs.

The Global Shape of the *trans* Form of the Ribozyme

First, we analyze the *trans* ribozyme folded in the presence of 10 mM Mg^{2+}. The full sequence of the construct is shown in Figure S1. It contains a perfectly paired 7 bp helix III in place of the natural 6 bp helix with a central bulge; we have previously shown that this ribozyme is almost fully active (Lafontaine et al., 2002). Also, GU base pairs of stem VI were replaced with GC pairs.

The shape of the *trans* VS is approximately cylindrical with a length of ~120 Å, with lateral protrusions (Figure 3A). The overall length agrees well with the maximum chord of D_{max} = 120 ± 10 Å, calculated from $P(r)$ transformation of the profile (see Experimental Procedures). The cylinder has a width of ~25 Å at its narrower points. The envelope accommodates the coaxial stacking of helices IV on III on VI, and is consistent with our earlier model of the *trans* ribozyme derived from FRET-based measurements on isolated junctions (Lafontaine et al., 2002), which gives a calculated end-to-end length of 130 Å.

We have also performed SAXS on variants of the *trans* VS, where helices IV or VI were extended by 10 and 11 bp, respectively, in separate constructs (see Figure S1). Both modifications resulted in significant increases (~10 Å) in R_g, consistent with the added helices being remote from the center of mass (Table 1). Moreover, the D_{max} values increased by 30–40 Å, as expected if the maximum chord is the end-to-end vector for the IV-III-VI stack.

Although the results are in good agreement with the coaxial stacking of helices IV, III, and VI in the *trans* ribozyme, the locations of helices II and V are less clear. According to our earlier model, these should extend laterally from the stacked helices. The protrusions do not permit us to position these helices with great confidence in the *trans* form of the ribozyme alone. The bead model derived from the *cis* construct did, however, allow us to locate these positions and then to transfer those positions back to the *trans* structure (see below).

The Global Shape of the Three-Helix Junctions in Isolation

We have further dissected the VS ribozyme into its component three-way helical junctions. We prepared junctions II-III-VI and
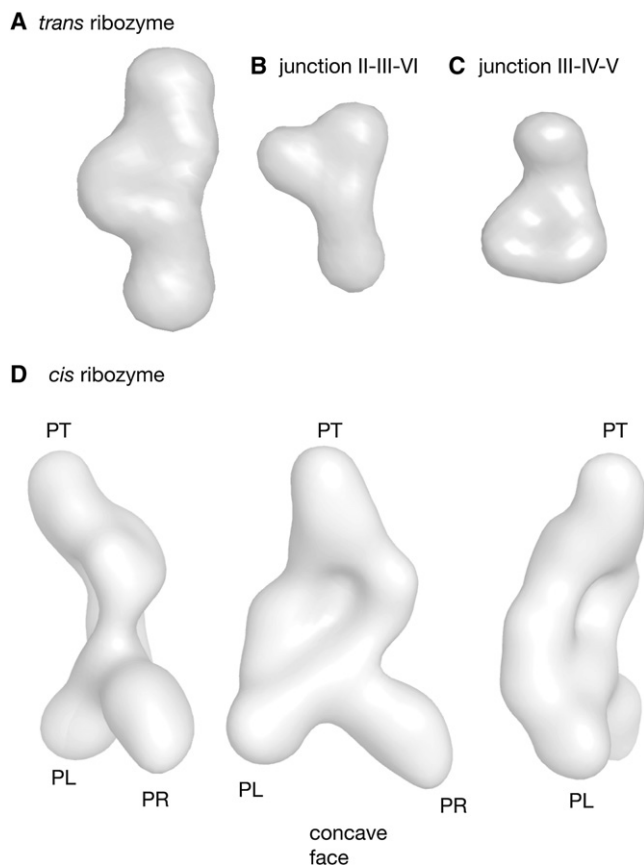
Figure 3. Electron Density Maps for the *cis* and *trans* Ribozymes, and the Two Isolated Three-Way Junctions Obtained from SAXS Measurements

(A) The *trans* VS ribozyme.
(B) The II-III-VI junction.
(C) The III-IV-V junction.
(D) Three views of the *cis* VS ribozyme. The central view shows the concave face. The three protuberances extend from the central flat box, labeled PL, PR, and PT. PR is the most prominent. The two side views are shown on the left and right. These clearly reveal the thinness of the envelope.

III-IV-V from single RNA species (Figure S1), generating junctions each with one open helix (II and III, respectively, with the latter extended to 10 bp) and the remaining two arms as stem-loop structures (Figures 3B and 3C). The A bulge was removed from helix III, but the remaining arms contained their natural loops and non-Watson-Crick pairs.

The low-resolution electron density maps of the two junctions in the presence of 20 mM Mg^{2+} ions have significantly irregular shapes, with protrusions that suggest helical arms. The II-III-VI junction (Figure 3B) has a longest arm with a width of ~25 Å, and a length of 50 Å, suggesting this is helix VI with a length of 13 bp plus its internal and terminal loops. This helix appears to be coaxial with the shortest arm, most likely helix III (5 bp), leaving helix II (8 bp plus bulge) as the laterally directed arm. Junction III-IV-V (Figure 3C) gave a triangular-shaped map, with a longest chord of ~70 Å. The shape suggests the presence of three helical arms, but we found that further progress with assignment of arms in both junctions could be best made in the context of the complete ribozyme, discussed below.

The Global Shape of the Complete *cis* Ribozyme

A low-resolution electron density map calculated from SAXS data for the *cis*-acting form of the ribozyme is shown in Figure 3D. The *cis* construct is closely similar to the natural form shown in Figure 1. The map was calculated using the scattering profiles obtained in the presence of 10 mM Mg^{2+}; however, data collected in 20 and 100 mM Mg^{2+} gave identical values for R_g and D_{max}, as well as very similar $P(r)$ distributions and structure reconstructions. Under conditions where the ribozymes are fully folded, both *cis* and *trans* forms have similar maximum chord lengths (Table 1). The electron density maps of the *cis* and *trans* forms reveal extended structures with maximum lengths of 125 Å, consistent with the D_{max} values. However, there are some significant differences between the two envelopes. The *cis* ribozyme has a central region in the form of a relatively flat box of ~50 Å square and a thickness of ~20 Å. Three protuberances radiate from the box, termed PT, PR, and PL (Figure 3D). The central box has a small degree of curvature, and we term the face that places the PL protuberance at the lower left as the concave face. The most obvious difference between the *cis* and *trans* structures is the presence of the new protuberance (PL) in the *cis* ribozyme, strongly suggesting the position of an additional helix. A ridge runs diagonally across the concave face, suggesting the path of a helix. The fitting of helices into this distinctive envelope is discussed in the following section.
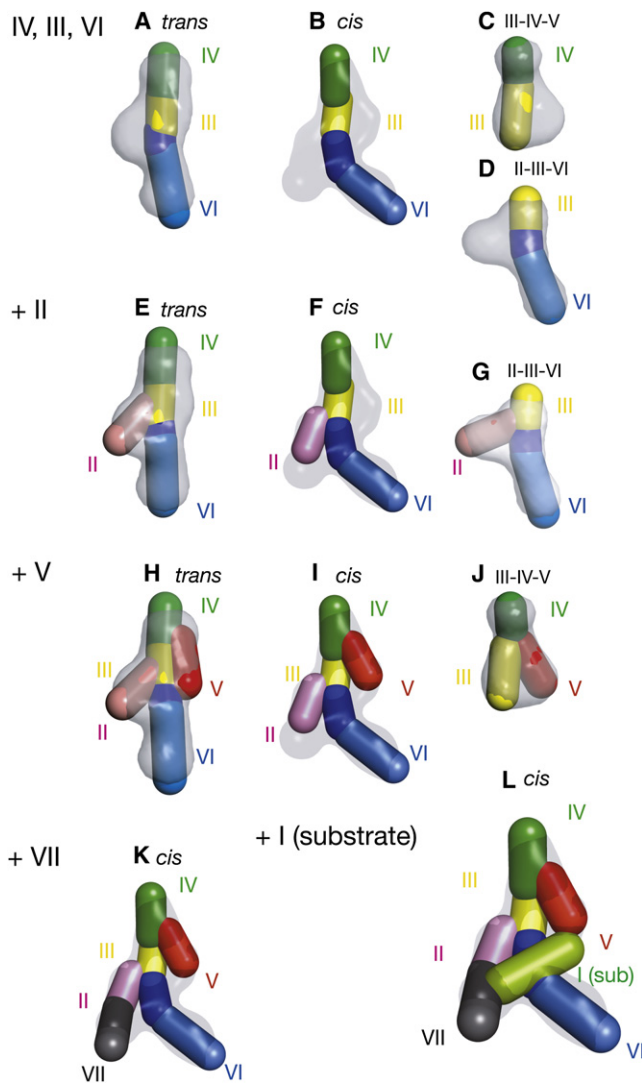
Fitting Helices into the Electron Density Maps

The irregular envelope of the electron density calculated for *cis* form of the ribozyme and its subcomponents places considerable limitations on how helices can be fitted, particularly in view of the overall length and a thickness that is close to that of a single helix. We have performed the fitting process using cylinders of appropriate length and diameter to represent individual helical sections.

Helices IV, III, and VI

We started the fitting process by placing cylinders corresponding to the coaxially aligned helices IV-III-VI along the longest vector—filling the protuberances PT and PR, running from top to bottom right viewed onto the concave face (Figure 4B). The assignment is consistent with the data for the *trans* ribozyme (above, and Figure 4A), and with our previous deduction of coaxial alignment of helices IV-III-VI (Lafontaine et al., 2002). We have represented helix VI by two cylindrical sections connected by a flexible joint to allow for a change of trajectory at an internal loop. In fitting the density, helices IV and III and the first section of VI are coaxial, but we found it necessary to introduce a bend (with an included angle ~130°) into helix VI to accommodate the electron density of the *cis* ribozyme. The distortion of helix VI suggests a local change in structure arising from interaction with the additional helical segments, probably the substrate stem-loop I (discussed below). The subsections of helices IV-III and III-VI can also be fitted well into the electron density maps of the III-IV-V and II-III-VI junctions, respectively (Figures 4C and 4D).

Helix II

Helix II forms a three-way junction with helices III and VI, locating one end of the helix in the structure. Having placed the coaxially stacked helices IV-III-VI into the electron density of the *cis*

Figure 4. Sequential Fitting of RNA Segments into the Electron Density Maps

The RNA helices are represented by cylinders of appropriate length and 22 Å diameter. The electron density envelopes are arranged so that in the top three rows the *cis* ribozyme is central, with the *trans* ribozyme on the left and the isolated junctions on the right. The first row shows the fitting of a coaxial alignment of helices IV-II-VI into the longest vector in all structures, most significantly from PT to PR in the *cis* ribozyme. In the following two rows, helices II then V are added. In the bottom row, helix VII is fitted into the PL protuberance (shown on the left). Finally, the substrate helix I is fitted in the structure shown on the right. The color coding of helices matches that of the secondary structure (Figure 1).

ribozyme to form the backbone of the structure, this leaves a space on the left side of the flat box that well accommodates helix II directed toward PL (Figure 4F). This disposition of the II-III-VI junction also fits well with the density for the *trans* ribozyme (Figure 4E) and the isolated junction (Figure 4G).

Helix V

The location of helices IV, III, VI, and II leaves vacant electron density to the right-hand side into which helix V can be placed,

to form a three-way junction with helices III and IV (Figure 4I). The resulting trajectory of helix V makes an acute angle (∼40°) with helix III. The deduced structure for the III-IV-V junction also fits well with the density for the *trans* ribozyme (Figure 4H) and the isolated junction (Figure 4J).

Helix VII and the Substrate Stem-Loop

The location of helix VII is now obvious as the remaining vacant lobe (PL) of the electron density extending bottom left in the *cis* ribozyme (Figure 4K). This now just leaves the substrate stem-loop I to be located. In the *cis* ribozyme, the substrate forms an additional three-way junction with helices II and VII, while making a loop-loop interaction at its other end with helix V (Rastogi et al., 1996). If we place the substrate helix onto the structure to satisfy these requirements it then occupies the ridge of density forming the lower-right edge of the box (Figure 4L). In addition, this allows the cleavage site to be located in close proximity to the A730 loop (the deduced active site) on helix VI. The envelope of electron density at the point at which helices I and VI are juxtaposed is barely over one helix thick, suggesting an intimate melding of the two helices. This is expected to create the chemical environment in which catalysis can occur.

In the course of these studies, we explored many alternative ways in which to fit the cylinders into the electron density map, but the model in Figure 4 is the one providing the best fit for all the cylinders.

Comparison with Earlier Models

The global way in which the SAXS-derived maps of the *cis* ribozyme and its components were fitted simultaneously provides confidence in the new model. It contains most of the features of our previous model that was based upon analysis of the elements of the structure, especially the three-way helical junctions (Lafontaine et al., 2002). Variation of D_{max} of the *trans* ribozyme with extensions in stems IV and VI (Table 1) firmly establish the coaxially aligned helices IV-III-VI, and the end-to-end distance calculated for that assembly is in good agreement with the D_{max} and the longest length of the electron density map that are 115 and 129 Å, respectively, for the *trans* and the *cis* ribozymes.

The new model also contains laterally directed helices II and V. This introduces a chirality into the structure, and a complication in using bead reconstructions is the generation of mirror images. The X-ray scattering data provide information on interatomic distances, but there is no inherent discrimination between mirror images. Our previous electrophoretic analysis had provided an estimate of the dihedral angle formed by helices II, III, and V, and perhaps more importantly had given the direction of change in dihedral angle as the length of helix III was increased. The variation of dihedral angle with helix III length effectively references the structure to the handedness of that helix (Lafontaine et al., 2002). This provides a means of mirror-image discrimination of the bead reconstructions when the positions of helices II and V are defined, which is clearly possible in the *cis* ribozyme. This chiral discrimination firmly places the substrate interactions on the concave face of the electron density of the *cis* ribozyme. The absolute value of the dihedral angle (helices II, III, V) appears to be larger in the SAXS-derived model. However, the value of the dihedral angle deduced from the electrophoretic

experiments is very sensitive to the trajectory of helix III. Small changes to the relative trajectory of this short helix could be made within the confines of the electron density, leading to a dihedral angle that was compatible with the previous estimation. The new model explains the rather low degree of modulation observed in the electrophoretic analysis (Lafontaine et al., 2002) used to define the dihedral angle, arising from the rather small angle subtended between helices III and V.

By comparison with some ribozymes, our deduced structure of the VS ribozyme is relatively open, suggesting that most of the RNA would be accessible to the solvent. This is consistent with hydroxyl radical cleavage mapping on a *cis* form of the VS ribozyme (Hiley and Collins, 2001), where protected regions were mostly very short and not strongly protected. This contrasts with the glmS ribozyme, for example; this has a much more globular fold (Klein and Ferré-D'Amaré, 2006; Cochrane et al., 2007), resulting in significant regions of strong protection against radical cleavage (Hampel and Tinsley, 2006). Although the absence of helix VII in the VS ribozyme construct used by Hiley and Collins (Hiley and Collins, 2001) prevents exact comparisons with our data, we note that some protection was observed in helix II and in the section of the II-III-VI junction connecting helices III and VI. Protection was also observed in the region of helix VI close to A756.

The geometry deduced for the two three-way junctions of the core ribozyme fits well with the structures of related junctions found in the structures of the ribosome. The global structure of the II-III-VI junction fits that of a $2HS_5HS_3$ junction formed by helices 5, 6, and 7 of 23S rRNA. We have previously demonstrated that the ribosomal sequence can be substituted in the VS ribozyme with only a small reduction of catalytic activity (Lafontaine et al., 2001a). Interestingly, there is an $HS_1HS_5HS_2$ junction of quite similar global structure to the III-IV-V junction occurring in the 23S rRNA (helices 90, 91, and 92). The helices equivalent to III and V are almost side by side, as we have now deduced for the ribozyme. The first three nucleotides of the 5 nt single-stranded section adopts a UNR turn in the ribosomal junction, as previously proposed for the VS junction (Sood and Collins, 2001). This loop contains a single base pair, so it might formally be regarded as a kind of four-way junction; interestingly, it was shown that the loop could be replaced with a fourth helix with retention of catalytic activity (Sood and Collins, 2001).

Construction of a Model of the VS Ribozyme

We have constructed a model of the complete *cis*-acting form of the VS ribozyme using the cylinder model described above as a starting point. This exercise was performed to see whether a stereochemically acceptable model based upon the SAXS-derived structure could be constructed that would be consistent with all the available data. A number of aspects of the structure are presently unknown, and the resulting model should not be confused with an atomic-resolution structure. However, it has heuristic value upon which future experiments on the folding and function of the ribozyme may be based.

We have replaced the cylinders with RNA helices manually located to fit the electron density envelope. In most cases, these were canonical A-form helices (exceptions are described in Experimental Procedures) and were treated as rigid bodies in what follows.

Turning to the tertiary structure of the ribozyme, the two three-way helical junctions organize the core of the structure. The center of junction II-III-VI was modeled using the ribosomal nucleotides from junction 5-6-7 discussed above. The insertion of the other ribosomal junction (helices 90, 91, and 92) at the junction III-IV-V location caused a steric clash between the end of stem V and stem III. This junction was therefore constructed manually. The inclusion of the junctions also largely determines the rotational settings of helices II–VI. The three-way junction between helices I, II, and VII will play an important role in determining the trajectory of the substrate helix I. Unfortunately, there are few clues to the structure of this junction, and therefore no specific structure could be incorporated into the model prior to energy minimization. Single-stranded nucleotides were located to link the termini of the different stems. The loop-loop interaction between helices I and V is well established (Rastogi et al., 1996), and was included as a distance restraint in the modeling process. Last, there is good evidence for a direct role of A756 in the cleavage of the scissile phosphate (Lafontaine et al., 2001b; Sood and Collins, 2002) and their physical proximity (Hiley et al., 2002), and we have therefore included this as an additional restraint in our modeling.

The structure of this model was refined in an iterative manner involving manual adjustment and energy minimization using XPLOR-NIH 2.18. Single unpaired nucleotides were incorporated at approximate positions and refined using a simplified energy function within XPLOR represented by repulsive-only van der Waals, bond, angle, and dihedral terms. Each independent helix was treated as a rigid body, as were single nucleotides linking helices, including the nucleotides from junction II-III-VI. Theoretical scattering profiles were calculated from the 3D atomic models using the program CRYSOL (Svergun et al., 1995) and compared with the experimental data. XPLOR-NIH and CRYSOL were used iteratively until the experimental and calculated profiles achieved the best agreement possible (Figure S4B).

Due to the large number of variables within an all-atom model, even after simplification of the refinement by definition of rigid bodies, a number of similar models of the complete ribozyme were generated by this process. The best of these was selected on the basis of stereochemistry, back-calculated fit to the experimental data, and the extent of enclosure by the bead-reconstruction-derived electron density envelope. The final model (Figure 5) demonstrates that a stereochemically acceptable atomic model can be built that conforms to the electron density envelope calculated from the SAXS profile. The model has $R_g = 37$ Å and $D_{max} = 128$ Å, which are in reasonable agreement with those calculated from the SAXS data of 39 ± 0.1 Å and 120 ± 5 Å, respectively.

The gross shape of the structure remains closely similar to the cylinder model. The fitting of the electron density very naturally brings the internal loop of the substrate helix I into juxtaposition with the A730 loop of helix VI. Hiley et al. (2002) showed that position 621 adjacent to the cleavage position in the substrate could be crosslinked with A756 in the A730 loop. We have no atomic-level information on the nature of the interaction, so this cannot be modeled in any detail. But the intimate contact between these helices is consistent with our previous conclusion that the active site requires the participation of nucleobases from both helix I (G638 in the substrate loop) and helix VI (A756 in the
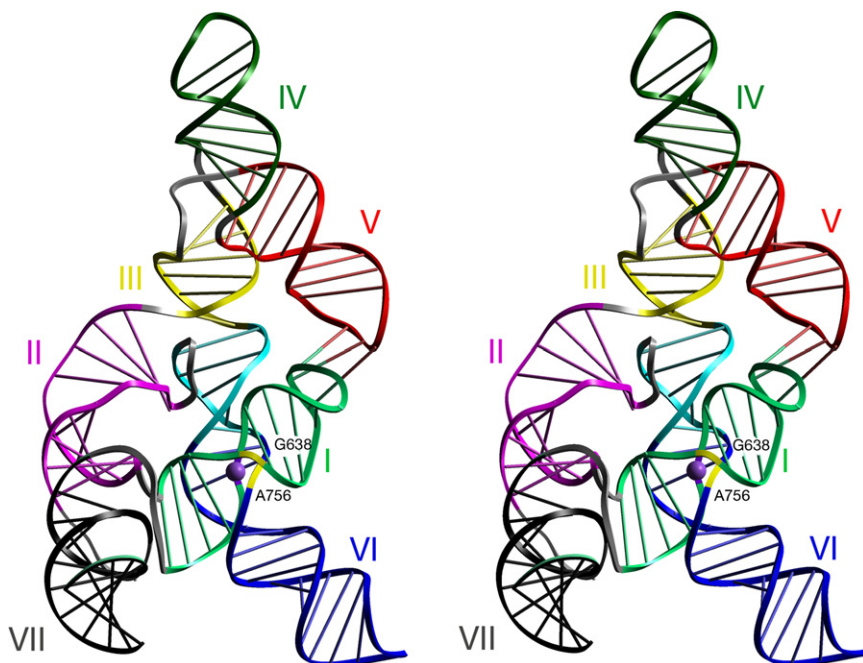
Figure 5. Parallel-Eye Stereoscopic Image of a Model of the Complete VS Ribozyme
The model was constructed by connecting the previously defined, helical sections of the low-resolution model shown in Figure 4. Energy-minimization refinement against the standard stereochemical restraints was used to regularize and refine the structure. The path of the backbone is indicated by the ribbon, and the positions of base pairs are indicated by the bars. The color coding of helices matches that of the secondary structure (Figure 1). The scissile phosphate is shown by the purple ball, and the probable active site components A756 and G638 are highlighted in yellow.

A730 loop), and this interaction could be responsible for a change in the trajectory of the axis of helix VI. The association of the loops evidently creates the environment that permits the catalysis of the *trans*-esterification reactions, and we have recently provided evidence consistent with general acid-base catalysis by the nucleobases of A756 and G638 (Wilson et al., 2007). Many of these characteristics are strikingly similar to those of the hairpin ribozyme.

The Docking of the Substrate Stem-Loop to Form the Active Site, and the Role of the I-II-VII Junction

In the course of these studies, we have collected scattering data from a simple *cis* form of the ribozyme lacking helix VII (data not shown). However, we observed changes in the scattering profile over the 20–100 mM range of Mg^{2+} ion concentration range, and bead reconstructions failed to provide a consistent description of the shape, and we concluded that this form was probably too dynamic to be amenable to ab initio structure reconstruction. The addition of helix VII gives greatly improved data, and the positions of all helical segments are clearly defined. The ridge of density running from the I-II-VII junction to the end of helix V is most probably the substrate but the space enclosed seems to be smaller than would be required for a full helix crossing in front of helix VI. This may in part be due to intimate melding between helices I and VI, but may also reflect some residual dynamics in the docking. A fraction of ribozyme with undocked substrate would lead to an increase in R_g, and we note that our model underestimates the R_g by 2 Å. Nevertheless, the results suggest that the formation of the additional three-way junction formed by helices I, II, and VII helps to stabilize the fold.

The role of helix VII may be similar to the auxiliary folding domains of other nucleolytic ribozymes. Recently, it has emerged that a number of these ribozymes have peripheral structural features that are dispensable for basic catalytic activity but nevertheless important for function under physiological conditions. This was first discovered for the hammerhead ribozyme, where loop-loop interactions between helices I and II resulted in activity (Khvorova et al., 2003) and folding (Penedo et al., 2004) at lower divalent ion concentrations, potentially faster cleavage reactions (Canny et al., 2004), and a facilitated ligation reaction. Similarly, the four-way junction of the hairpin ribozyme, although not essential for cleavage activity, facilitates folding at much reduced divalent ion concentrations (Murchie et al., 1998; Walter et al., 1999; Tan et al., 2003) and allows ligation reactions to occur (Fedor, 1999). It appears that the addition of helix VII and the consequent formation of a new three-way helical junction plays a similar role in the VS ribozyme.

Conclusion

We have derived a low-resolution model of the complete VS ribozyme from solution scattering experiments. The structure emerges from a synthesis based upon data derived from the fully intact RNA and its components, in contrast to our earlier studies in which the structure was reconstructed solely from its isolated components (the so-called divide-and-conquer approach). Yet the new structure agrees very well with the earlier model, being built upon essentially the same core of helices II–VI. The three-way helical junctions all play key roles in directing the architecture of the ribozyme. The low-resolution electron density envelope is good enough to fit cylindrical representations of helical segments, and has provided a starting point for more detailed structural modeling of the VS ribozyme to include the junctions and tertiary interactions. The SAXS data provide physical evidence for the location of the substrate within the ribozyme, showing that close interaction between the substrate loop and the A_{730} loop is very achievable in the context of this structure. This conforms very well to our current mechanistic ideas, in which a significant element of the catalysis of phosphoryl transfer arises by general acid-base catalysis by the nucleobases of A756 and G638. In addition, the new structure provides some clues to the function of the additional helix VII in the formation of the active complex. Finally, this study highlights the power of X-ray scattering to provide valuable insight into the structure of a relatively complex folded RNA species.

EXPERIMENTAL PROCEDURES

RNA Synthesis and Preparation of RNA Constructs

Templates for RNA synthesis were generated by PCR reactions using synthetic DNA oligonucleotides. PCR reactions were carried out using KOD DNA polymerase (Novagen), with 100 μM primers and 1 μM synthetic template for 30 cycles with an annealing temperature ranging from 50°C to 55°C. Transcription reactions were performed for 2 hr at 37°C using 20 μM template in the presence of 40 mM Tris-HCl (pH 8.0), 20 mM $MgCl_2$, 2 mM spermidine, 4 mM of each NTP (Roche), 0.1 U of pyrophosphatase (Sigma), 0.01% Triton X-100 (Sigma), and T7 RNA polymerase. Transcribed RNA was purified by electrophoresis in 4%–8% polyacrylamide in the presence of 7 M urea, and recovered by electroelution into ammonium acetate from excised gel fragments and by precipitation in ethanol.

SAXS Measurements

All SAXS measurements were carried out at undulator beamline BESSRC CAT 12-ID of the Advanced Photon Source, Argonne, IL, USA. The measurements employed a sample-detector distance of 2 m, a CCD detector (MAR USA) readout, and a custom-made sample holder (Lipfert et al., 2006). The X-ray energy for all measurements was 12 keV, corresponding to an X-ray wavelength of 1 Å. Details of the measurements and beamline are as described previously (Lipfert et al., 2006; Beno et al., 2001; Seifert et al., 2000).

SAXS data were collected at RNA concentrations ranging from 0.5 to 4.5 mg/ml in 100 mM Tris-HCl (pH 8.0) with 25 mM KCl and varying amounts of $MgCl_2$ added. Samples were thawed and centrifuged for 10 min at 11,000 g immediately before data collection. Five exposures each of 2.0 s were made for each condition. The data were image corrected, normalized by incident flux, and circularly averaged, and the five profiles were averaged to improve signal quality. Appropriate buffer profiles were collected using identical procedures and subtracted for background correction. The data showed no signs of radiation damage, as tested by comparing scattering profiles of subsequent exposures on the same sample.

SAXS Data Analysis

Scattering intensities were recorded as a function of the momentum transfer q, with $q = 4\pi \sin(\theta)/\lambda$ (where 2θ is the total scattering angle) and λ the X-ray wavelength, in the range of $q = 0.019$–0.28 Å^{-1}. The program GNOM (Svergun, 1992) was used to perform regularized indirect transforms of the scattering data to obtain $P(r)$ functions (a histogram of interatomic distances). The $P(r)$ function has a maximum at the most probable intermolecular distance and goes to zero at D_{max}, the maximum intramolecular distance. For each measured scattering profile, regularized transforms are performed with the input parameter D_{max} varied in steps of 2 Å. Values of D_{max} were chosen that yielded solutions that (1) fit the experimental data well and (2) have a smooth and strictly positive $P(r)$ function. From this procedure, values for D_{max} and the radius of gyration R_g

$$R_g = \frac{\int_0^{D_{max}} r^2 P(r)dr}{2\int_0^{D_{max}} P(r)dr} \tag{2}$$

were obtained for each of the measurements. Guinier analysis (Guinier, 1939) of the low q data provides alternative estimates of the R_g, which agree with the values found from the $P(r)$ functions.

Ab Initio 3D Shape Reconstructions

We used the program DAMMIN (Svergun, 1999) to construct 3D bead models that fit the scattering data. DAMMIN employs a simulated annealing procedure and a "compactness criterion," and its applicability to RNA has been recently demonstrated (Lipfert et al., 2007a, 2007b) . Ten independent DAMMIN runs were performed for each scattering profile in the "slow" mode, using default parameters and no symmetry assumptions (P1 symmetry). The initial search volumes were chosen to be spheres with diameters corresponding to the maximum chord D_{max} of the corresponding construct plus 20 Å. Use of cylindrical search volumes gave very similar results.

The models resulting from independent runs were superimposed using the program SUPCOMB (Kozin and Svergun, 2001), which performs an initial alignment of structures based on their axes of inertia followed by minimization of the normalized spatial discrepancy (NSD). The NSD has the property that it is zero for identical objects and larger than 1 for objects that systematically differ from one another (Kozin and Svergun, 2001). For all VS constructs described here, we consistently found NSD values < 1 when comparing the independent reconstructions runs, indicating that the algorithm converges to reproducible and structurally similar solutions. The aligned structures were averaged using the program DAMAVER (Volkov and Svergun, 2003), giving an effective occupancy of each voxel. Keeping all occupied voxels generates a convex hull of all models. Filtering at half-maximal occupancy provides "filtered" models that were used for all subsequent analyses.

To provide a clearer representation of the structures, the low-resolution overall shape comprising individual dummy atoms was converted to a density map. Structure factors were calculated from the bead model using SFALL from the CCP4 program suite (CCP4, 1994), generating an MTZ file. In order to display the electron density map in PyMOL (DeLano, 2002), MTZ files were successively converted to an XPLOR-NIH-compatible format and then to a PyMOL-compatible format; the scripts used are available on the website below.

Construction of Models

Electron density maps were initially fitted by manual insertion of cylinders of appropriate radius and length to represent the helical segments in a sequential manner as described in the text and shown in Figure 4. The cylinder model of the cis VS construct was then used as the basis for constructing an all-atom model of the ribozyme. The cylinders were replaced by idealized helices constructed using either InsightII (Accelrys) or Coot (Emsley and Cowtan, 2004), except for helices VI and I where NMR structures were used (Flinders and Dieckmann, 2004; Hoffmann et al., 2003) In the other stems, non-Watson-Crick base pairs were approximated as follows. In stem V, the G•U wobble base pairs were replaced with GC base pairs. The A bulge of stem II was incorporated as a stacked nucleotide (although deletion is detrimental to activity, its replacement by a base pair only has a small effect); the structure was taken from nucleotides 262–264 and 311–312 from Protein Data Bank ID code 1GRZ, where an intercalated A is surrounded by a CG and a GC base pair. The single-stranded nucleotides and the flanking two base pairs of each stem from the junction II-III-VI were substituted (with suitable modification) with the nucleotides from the ribosomal structure corresponding to helices 5, 6, and 7 of 23S rRNA as discussed previously (Lafontaine et al., 2001a).

Once the seven helical stems and junction II-III-VI were positioned, the single-stranded nucleotides linking the stems were incorporated at approximate positions until the 199 nucleotides were present in the model. Minimization was performed with a rigid-body strategy using XPLOR-NIH 2.18 (Schwieters et al., 2003). Each stem, as well as each of the single-stranded nucleotides, were defined as rigid bodies. Other known structural features were incorporated. The interaction between loops I and V was enforced using distance restraints (Rastogi et al., 1996), and the cleavage site on stem I was constrained to be close to the predicted active site on stem VI at nucleotide A756 (Lafontaine et al., 2001b; Hiley et al., 2002). Refinement was performed using a simplified energy function represented by terms for repulsive-only van der Waals, bond, angle, and dihedral energies.

The coordinates of the atomic model were input to CRYSOL (Svergun et al., 1995) to backcalculate a 1D SAXS profile from the 3D structures. XPLOR-NIH and CRYSOL and manual manipulation were used in an iterative fashion until the backcalculated profile of the atomic model gave a reasonable fit to the experimental SAXS data. It should be noted that the iterative refinement also took into account the fit to the calculated electron density envelope. Due to the level of unknown structural detail within parts of the atomic model, agreement with the SAXS restraint within XPLOR-NIH, good backcalculation to the full Kratky plots, and overall structural agreement with the calculate electron density was given preference over local covalent geometry.

Viewing the Models of the Ribozyme and Its Components

The models can be viewed interactively using Jmol at http://www.dundee.ac.uk/biocentre/nasg/vs. A visual description of the conversion of the scattering profile to a 3D density map, superposition of the different density maps, and scripts are also available at this website.

SUPPLEMENTAL DATA

ACKNOWLEDGMENTS

REFERENCES

Beattie, T.L., Olive, J.E., and Collins, R.A. (1995). A secondary-structure model for the self-cleaving region of *Neurospora* VS RNA. Proc. Natl. Acad. Sci. USA *92*, 4686–4690.

Beno, M.A., Jennings, G., Engbretson, M., Knapp, G.S., Kurtz, C., Zabransky, B., Linton, J., Seifert, S., Wiley, C., and Montano, P.A. (2001). Basic energy sciences synchrotron radiation center undulator sector at the Advanced Photon Source. Nucl. Instrum. Methods Phys. Res. A *467*, 690–693.

Canny, M.D., Jucker, F.M., Kellogg, E., Khvorova, A., Jayasena, S.D., and Pardi, A. (2004). Fast cleavage kinetics of a natural hammerhead ribozyme. J. Am. Chem. Soc. *126*, 10848–10849.

CCP4 (Collaborative Computational Project, Number 4) (1994). The CCP4 suite: programs for protein crystallography. Acta Crystallogr. D Biol. Crystallogr. *50*, 760–763.

Cochrane, J.C., Lipchock, S.V., and Strobel, S.A. (2007). Structural investigation of the GlmS ribozyme bound to its catalytic cofactor. Chem. Biol. *14*, 97–105.

DeLano, W.L. (2002). The PyMOL Molecular Graphics System (Palo Alto, CA: DeLano Scientific).

Doniach, S. (2001). Changes in biomolecular conformations seen by small angle X-ray scattering. Chem. Rev. *101*, 1763–1778.

Emsley, P., and Cowtan, K. (2004). Coot: model-building tools for molecular graphics. Acta Crystallogr. D Biol. Crystallogr. *60*, 2126–2132.

Fedor, M.J. (1999). Tertiary structure stabilization promotes hairpin ribozyme ligation. Biochemistry *38*, 11040–11050.

Flinders, J., and Dieckmann, T. (2004). The solution structure of the VS ribozyme active site loop reveals a dynamic "hot-spot." J. Mol. Biol. *341*, 935–949.

Guinier, A. (1939). La diffraction des rayons X aux trés petits angles: application à l'étude de phénomènes ultramicroscopiques. Ann. Phys. *12*, 161–237.

Guo, H.C.T., and Collins, R.A. (1995). Efficient *trans*-cleavage of a stem-loop RNA substrate by a ribozyme derived from *Neurospora* VS RNA. EMBO J. *14*, 368–376.

Hampel, K.J., and Tinsley, M.M. (2006). Evidence for preorganization of the glmS ribozyme ligand binding pocket. Biochemistry *45*, 7861–7871.

Hiley, S.L., and Collins, R.A. (2001). Rapid formation of a solvent-inaccessible core in the *Neurospora* Varkud satellite ribozyme. EMBO J. *20*, 5461–5469.

Hiley, S.L., Sood, V.D., Fan, J., and Collins, R.A. (2002). 4-thio-U cross-linking identifies the active site of the VS ribozyme. EMBO J. *21*, 4691–4698.

Hoffmann, B., Mitchell, G.T., Gendron, P., Major, F., Andersen, A.A., Collins, R.A., and Legault, P. (2003). NMR structure of the active conformation of the Varkud satellite ribozyme cleavage site. Proc. Natl. Acad. Sci. USA *100*, 7003–7008.

Jones, F.D., and Strobel, S.A. (2003). Ionization of a critical adenosine residue in the *Neurospora* Varkud satellite ribozyme active site. Biochemistry *42*, 4265–4276.

Jones, F.D., Ryder, S.P., and Strobel, S.A. (2001). An efficient ligation reaction promoted by a Varkud satellite ribozyme with extended 5′- and 3′-termini. Nucleic Acids Res. *29*, 5115–5120.

Khvorova, A., Lescoute, A., Westhof, E., and Jayasena, S.D. (2003). Sequence elements outside the hammerhead ribozyme catalytic core enable intracellular activity. Nat. Struct. Biol. *10*, 708–712.

Klein, D.J., and Ferré-D'Amaré, A.R. (2006). Structural basis of glmS ribozyme activation by glucosamine-6-phosphate. Science *313*, 1752–1756.

Kozin, M.B., and Svergun, D.I. (2001). Automated matching of high- and low-resolution structural models. J. Appl. Crystallogr. *34*, 33–41.

Lafontaine, D.A., Norman, D.G., and Lilley, D.M.J. (2001a). Structure, folding, and activity of the VS ribozyme: importance of the 2-3-6 helical junction. EMBO J. *20*, 1415–1424.

Lafontaine, D.A., Wilson, T.J., Norman, D.G., and Lilley, D.M.J. (2001b). The A730 loop is an important component of the active site of the VS ribozyme. J. Mol. Biol. *312*, 663–674.

Lafontaine, D.A., Norman, D.G., and Lilley, D.M.J. (2002). The global structure of the VS ribozyme. EMBO J. *21*, 2461–2471.

Lescoute, A., and Westhof, E. (2006). Topology of three-way junctions in folded RNAs. RNA *12*, 83–93.

Lilley, D.M.J., and Eckstein, F., eds. (2008). Ribozymes and RNA Catalysis (Cambridge, UK: Royal Society of Chemistry).

Lipfert, J., and Doniach, S. (2007). Small-angle X-ray scattering from RNA, proteins, and protein complexes. Annu. Rev. Biophys. Biomol. Struct. *36*, 307–327.

Lipfert, J., Millett, I.S., Seifert, S., and Doniach, S. (2006). Sample holder for small-angle X-ray scattering static and flow cell measurements. Rev. Sci. Instrum. *77*, 461081–461084.

Lipfert, J., Chu, V.B., Bai, Y., Herschlag, D., and Doniach, S. (2007a). Low resolution models for nucleic acids from small-angle X-ray scattering with applications to electrostatic modeling. J. Appl. Crystallogr. *40*, S229–S235.

Lipfert, J., Das, R., Chu, V.B., Kudaravalli, M., Boyd, N., Herschlag, D., and Doniach, S. (2007b). Structural transitions and thermodynamics of a glycine-dependent riboswitch from *Vibrio cholerae*. J. Mol. Biol. *365*, 1393–1406.

McLeod, A.C., and Lilley, D.M.J. (2004). Efficient, pH-dependent RNA ligation by the VS ribozyme in *trans*. Biochemistry *43*, 1118–1125.

Murchie, A.I.H., Thomson, J.B., Walter, F., and Lilley, D.M.J. (1998). Folding of the hairpin ribozyme in its natural conformation achieves close physical proximity of the loops. Mol. Cell *1*, 873–881.

Penedo, J.C., Wilson, T.J., Jayasena, S.D., Khvorova, A., and Lilley, D.M.J. (2004). Folding of the natural hammerhead ribozyme is enhanced by interaction of auxiliary elements. RNA *10*, 880–888.

Rastogi, T., Beattie, T.L., Olive, J.E., and Collins, R.A. (1996). A long-range pseudoknot is required for activity of the *Neurospora* VS ribozyme. EMBO J. *15*, 2820–2825.

Saville, B.J., and Collins, R.A. (1990). A site-specific self-cleavage reaction performed by a novel RNA in *Neurospora* mitochondria. Cell *61*, 685–696.

Schwieters, C.D., Kuszewski, J.J., Tjandra, N., and Clore, G.M. (2003). The Xplor-NIH NMR molecular structure determination package. J. Magn. Reson. *160*, 65–73.

Seifert, S., Winans, R.E., Tiede, D.M., and Thiyagarajan, P. (2000). Design and performance of a ASAXS instrument at the Advanced Photon Source. J. Appl. Crystallogr. *33*, 782–784.

Sood, V.D., and Collins, R.A. (2001). Functional equivalence of the uridine turn and the hairpin as building blocks of tertiary structure in the *Neurospora* VS ribozyme. J. Mol. Biol. *313*, 1013–1019.

Sood, V.D., and Collins, R.A. (2002). Identification of the catalytic subdomain of the VS ribozyme and evidence for remarkable sequence tolerance in the active site loop. J. Mol. Biol. *320*, 443–454.

Svergun, D.I. (1992). Determination of the regularization parameter in indirect-transform methods using perceptual criteria. J. Appl. Crystallogr. *25*, 495–503.

Svergun, D.I. (1999). Restoring low resolution structure of biological macromolecules from solution scattering using simulated annealing. Biophys. J. *76*, 2879–2886.

Svergun, D.I., and Koch, M.H.J. (2003). Small-angle scattering studies of biological macromolecules in solution. Rep. Prog. Phys. *66*, 1735–1782.

Svergun, D.I., Barberato, C., and Koch, M.H.J. (1995). CRYSOL—a program to evaluate X-ray solution scattering of biological macromolecules from atomic coordinates. J. Appl. Crystallogr. *28*, 768–773.

Tan, E., Wilson, T.J., Nahas, M.K., Clegg, R.M., Lilley, D.M.J., and Ha, T. (2003). A four-way junction accelerates hairpin ribozyme folding via a discrete intermediate. Proc. Natl. Acad. Sci. USA *100*, 9308–9313.

Volkov, V.V., and Svergun, D.I. (2003). Uniqueness of ab initio shape determination in small-angle scattering. J. Appl. Crystallogr. *36*, 860–864.

Walter, N.G., Burke, J.M., and Millar, D.P. (1999). Stability of hairpin ribozyme tertiary structure is governed by the interdomain junction. Nat. Struct. Biol. *6*, 544–549.

Wilson, T.J., McLeod, A.C., and Lilley, D.M.J. (2007). A guanine nucleobase important for catalysis by the VS ribozyme. EMBO J. *26*, 2489–2500.

Zhao, Z.Y., McLeod, A., Harusawa, S., Araki, L., Yamaguchi, M., Kurihara, T., and Lilley, D.M.J. (2005). Nucleobase participation in ribozyme catalysis. J. Am. Chem. Soc. *127*, 5026–5027.